Myeloid-instructed CD14$^+$CD4$^+$ T cells within the tumor microenvironment are associated with TNFα signaling and prolonged survival in non-small cell lung cancer

Claire Marceaux[1,4], Kenta Yokote[1], Velimir Gayevskiy[1], Daniel Batey[1], Ilariya Tarasova [3,5], Laurie Choux[1], Lucy Riley[1], Nina Tubau Ribera[2], Jack Hywood[7], Michael Christie[7], Phillip Antippa[6,7], Terence P Speed[3,5], Kelly L. Rogers[2,4], Belinda Phipson[3,5], and Marie-Liesse Asselin-Labat[1,4*].

[1]*Personalised Oncology Division,* [2]*Advanced Technology and Biology Division,* [3]*Bioinformatics Division; The Walter and Eliza Hall Institute of Medical Research, Parkville, Australia*

[4]*Department of Medical Biology,* [5]*School of Mathematics and Statistics,* [6]*Department of Surgery, The University of Melbourne, Parkville, Australia*

[7]*The Royal Melbourne Hospital, Parkville, Australia*

* corresponding authors: M-L. Asselin-Labat. labat@wehi.edu.au

Keywords:

Spatial proteomics

Spatial transcriptomics

Myeloid-instructed T cells

Non-small cell lung cancer

The authors declare no potential conflicts of interest.

Abstract

Immune cells from the adaptive and innate immune systems coexist in the tumor immune microenvironment (TME) to mediate tumor cell immunosurveillance and prevent tumor relapse. Relapse-free survival after surgical resection is heterogeneous in lung adenocarcinoma (LUAD) and lung squamous cell carcinoma (LUSC), the two major subtypes of non-small cell lung cancer. Yet, little is known about the composition and spatial organisation of the TME that could explain the different prognoses for lung cancer patients. Using spatial multi-omics analyses, we show that LUAD and LUSC have distinct TMEs and that neutrophil-enriched tumors are associated with worse survival, while the accumulation of myeloid-instructed $CD14^+$ T cells in the tumor core was associated with prolonged patient survival. $CD14^+CD4^+$ T cells express prototypic markers of myeloid cells and were found to be clonally expanded tumor-specific activated T cells. TNFα signaling was activated in tumors with high infiltration of $CD14^+CD4^+$ T cells in the tumor core. Our results demonstrate that innate immune cells impact adaptive immune cell activity to support the deployment of discrete T cell populations with anti-tumor activity.

Introduction

Histopathological analysis of cancer specimens is an essential part of clinical diagnosis to inform therapeutic decisions. Tissue architecture and cellular organisation provide a layer of information critical for pathologists to make informed diagnoses. Similarly, the characterisation of cell phenotypes and functional states in the physical context of a tumor is necessary to gain a broad understanding of cancer biology. This knowledge is essential in non-small cell lung cancer (NSCLC), where immunotherapy has improved patient outcomes, yet only 20% of patients respond to these treatments[1,2]. A comprehensive mapping of the complexity and heterogeneity of the cellular interactions in the tumor microenvironment (TME) driving tumor progression and relapse is still lacking, hindering the development of therapies tailored to the specific characteristics of individual tumor ecosystems.

Tumor cell molecular characteristics such as tumor mutational burden (TMB) and PDL1 expression are still heavily relied upon to determine patient prognostic and therapeutic approaches, yet recent studies demonstrate the importance of assessing the immune contexture to understand tumor evolution[3,4] and for prognostic and therapeutic purposes[5,6]. Exploratory analysis of Checkmate 227 clinical trial showed different response to treatments between the two main subtypes of NSCLC: Patients with advanced lung squamous cell carcinoma showed improved overall survival when treated with nivolumab + ipilimumab vs chemotherapy or nivolumab + chemotherapy vs chemotherapy, whereas increased overall survival was not observed in non-squamous lung adenocarcinoma (LUAD)[7,8]. These differences could be explained by differences in the TME of LUAD and LUSC. However, comparisons of the spatial organisation of the TME in LUAD and LUSC have been limited. Instead, analysis of immune cell composition and activity in NSCLC have been performed in small patient cohorts using single-cell transcriptomics combined with cell surface protein analyses[9–12]. Detailed evaluation of individual tumor cells and immune cells determined that the intersection between tumor cell-intrinsic factors, such as *TP53* mutation and TMB, combined with immune cell characteristics may be used to better predict response to immunotherapeutics[12]. However, these studies lack spatial resolution and information on how immune cell communities may influence tumor cell behaviours. Recent work by Sorin *et al.* utilised imaging mass cytometry to profile the TME in LUAD and revealed that specific immune cell neighborhoods composed of B cells and T helper cells were associated with better patient outcomes[13]. This study highlighted how cellular communities and their specific location, identified through spatial analysis, have a stronger biological impact than individual cells, and that evaluating this spatial organisation provides a

new layer of information, akin to that utilised in anatomical pathology for diagnosis, to decipher tumor biology. However, knowledge of the differences in the immune composition and spatial cell communities in the TME of LUAD and LUSC is still lacking.

Adaptive immunity is an essential component of the TME, and distinct subsets of T cells have been associated with better response to therapy and survival. In NSCLC, Corgnac *et al*. showed the accumulation of $CD8^+$ T cells with a tissue-resident memory phenotype (T_{RM}-like) in the tumor core was associated with response to immunotherapy in NSCLC[14]. $CD103^+CD8^+$ T_{RM}-like cells have been shown to play a role in tumor immunosurveillance and immune escape, indicating that T cell subsets exert distinct functions in mediating anti-tumor immunity[3,15,16]. More recently, Pallett *et al*. described a new subset of myeloid-instructed tissue-resident T cells present in the skin, lymph nodes, and liver. They showed that a subset of $CD8^+$, and in lower abundance $CD4^+$ T cells, expressed the TLR4 coreceptor CD14, a canonical marker of myeloid cells and innate immunity[17]. $CD14^+$ T cells expressed additional myeloid cell markers, including MHC-II and CD206, and constituted an immune-active subset of T cells in the human liver. These myeloid-instructed T cells were reprogrammed by the transfer of myeloid material to T cells upon direct contact of T cells with mononuclear phagocytes and were found to accumulate in hepatitis B virus-infected liver and in hepatocarcinoma[17]. The existence and contribution of these myeloid-instructed T cells to anti-tumor immunity in solid tumors is still unknown.

Here we applied multiplex ion beam imaging (MIBIscope) to a clinically annotated cohort of NSCLC patient samples. We designed a bespoke antibody panel to interrogate discrete immune cell populations and their spatial organisation in the TME of LUAD and LUSC, and their association with clinical outcomes. Importantly we integrated this spatial proteomics analysis with spatial transcriptomic approaches to provide a detailed mapping of the relationship between immune and tumor cells. We demonstrated the existence of a subset of clonally expanded T cells expressing the myeloid marker CD14. Infiltration of $CD14^+$ T cells in the tumor core correlated with tumor cells with an immunogenic phenotype and was associated with long-term patient survival. Overall, this study describes the existence of a discrete subset of tumor-infiltrating T cells that may be essential in driving anti-tumor immunity.

Results

A longitudinal cohort of resected NSCLC with survival outcome

To study the features of anti-tumor immunity associated with patient outcome in resectable NSCLC, we utilised our bank of 136 treatment-naïve NSCLC samples (stage I to IIIa) for which we had up to 10 years of longitudinal clinical follow-up (Fig 1A). To characterise the cellular traits of the TME that may be associated with prolonged survival, we selected tissue samples from patients with an overall survival of less than 3 years or more than 6 years post-surgery to perform spatial proteomics and spatial transcriptomics analyses. A total of 68 patients were analysed, comprising 28 samples with less than 3 years survival (21 LUAD and 7 LUSC) and 40 samples (26 LUAD and 14 LUSC) with more than 6 years survival (Figure 1A). H&E images were annotated by a pathologist to select regions of interest (ROIs) for spatial single-cell proteomics using the MIBIscope and spatial transcriptomics using whole transcriptome profiling on the GeoMx. On each ROI, GeoMx enabled the analysis of the gene expression profile of tumor cells exclusively (area of illumination (AOI) panCK$^+$ cells) and the immune compartment (AOI CD45$^+$ cells) (Fig 1B). After quality control checks, a total of 920 field-of-views (FOVs, average of 5 per patient) MIBI scans and 234 matched AOIs (average of 4 per patient) on GeoMx were selected for further analysis corresponding to 64 patients (44 LUAD and 20 LUSC; Fig 1A).

For spatial proteomic analysis, a bespoke panel of 38 conjugated antibodies was developed to identify tumor, immune cells and fibroblasts and detail their functional state. For each patient, multiple FOVs were scanned and stitched together to enable spatial analysis of cell communities in different tumor compartments: tumor core, tumor border and surrounding stroma, classified based on a pixel classifier trained in QuPath[18] (Fig 1B). Cells were segmented using a Deep Cell model[19] trained based on the expression of cytoplasmic (Major histocompatibility Complex Class I (MHC-I)), cell membrane (pan-cytokeratin (panCK)) and nuclei (dsDNA) markers. Individual cell phenotypes were manually annotated on 116 FOVs to train an XGboost machine learning method to phenotype twelve main cell types with an overall accuracy of 90%. A second independent model was developed for determining positive or negative expression of individual functional markers for each cell type. Using this approach, a total of 384,808 cells were classified into epithelial cells, fibroblasts and ten major immune cell subpopulations: B cells, CD4$^+$ conventional T cells, CD8$^+$ T cells, CD4$^+$ regulatory T cells, natural killer cells, gamma-delta T cells, macrophages, neutrophils, mast cells and dendritic cells. A heatmap of the mean expression of markers used for cell type annotation indicated a strong correlation between cell classification and the expression of expected markers (Fig 1C). Classified cells corresponded to 73% tumor cells, 21% immune cells and 6% stromal cells.

Unsupervised clustering of immune cells demonstrated the performance of our classification model with all lymphoid cells clustering away from myeloid cell subsets (Fig 1D). Consistent with previous publications utilising *in situ* methods or tissue dissociation approaches[3,11,13,20], the five most abundant immune cell types infiltrating NSCLC samples were B cells, $CD4^+$ conventional T cells, $CD8^+$ T cells, macrophages and neutrophils (Fig 1C).
Overall we have exploited a cohort of clinically annotated NSCLC samples to develop methods for tissue classification and cell-type phenotyping from single-cell multiplex protein imaging, and to interrogate the association between spatial proteomics and transcriptomics data with clinical outcomes.

Distinct spatial clusters of immune cells in the TME of LUAD and LUSC

We first investigated the characteristics of the tumor cells in LUAD and LUSC tissues. Consistent with previous studies[21,22], GeoMX analysis of $panCK^+$ tumor cell regions showed clear transcriptomic differences between LUAD and LUSC tumor cells as well as heterogeneity in the gene expression profile of tumor cells between patients of the same histological subtypes (Fig 2A). LUAD and LUSC expressed typical phenotypic markers of each histological subtypes (eg. *NKX2.1*, *KRT7*, *MUC1*, *SFTPB* in LUAD and *KRT5*, *KRT6*, *TP63* in LUSC;). With the proteomics analysis, we refined the coexpression of distinct functional markers in individual tumor cells. We observed a heterogenous pattern of expression of MHC-I and MHC-II in the two cancer subtypes (Fig 2B), consistent with previous studies where ~50% of tumors were found to have lost or have low levels of MHC-I and MHC-II[23,24]. MHC-I and MHC-II expressions were positively correlated in LUAD (Spearman correlation score: 0.7). Interestingly, loss of MHC-I was often associated with reduced expression of IFNγ (Spearman correlation score: 0.5) in LUAD tumor cells, but not in LUSC (Fig 2B). In LUSC, MHC-II expression was negatively associated with Ki67 expression (Spearman correlation score: -0.49). Expression of PDL1 in tumor cells varied across patients but was consistently lost in MHC-I negative tumors (Spearman correlation score: 0.32 in LUAD). IFNγ expression was low in all LUSC samples, except for one patient, whereas ~50% of LUAD tumors expressed IFNγ (Fig 2B). In LUAD, MHC-I/II^{low} tumors had less immune cell infiltration in the tumor core or border than MHC-I/II^{high} tumors. The tumor cell-specific expression of each of these markers, including PDL-1, was not associated with relapse-free survival or overall survival (Fig 2B).

We then compared the immune microenvironment of LUAD and LUSC samples. In both tumor subtypes, the predominant immune subsets in the whole tissue were $CD4^+$ and $CD8^+$ T cells, followed by B cells in LUAD, and macrophages in LUSC (Fig 2C). Analysis of the specific location of the cells in different tumor compartments – tumor core, tumor border or stroma – showed that immune cells were more frequent in the stroma. Within the immune cells, the proportions of distinct immune subsets were evenly distributed between the compartments or enriched in the stroma, except for macrophages and $CD8^+$ T cells that were more frequently detected in the tumor core and at the tumor border, in both LUAD and LUSC (Fig 2D and). Whole tissue analysis of immune cell infiltration revealed significantly higher B cell infiltration in the LUAD TME compared with LUSC, whereas neutrophils were more often present in LUSC. Detailed analysis of the TME in different compartments of the tumors highlighted that the enrichment for B cells in LUAD occurred at the border of the tumor front, while neutrophils were located at the border and in the stroma of LUSC (Fig 2E). In addition, this analysis of the different tumor compartments highlighted further differences between the two histological subtypes where dendritic cells were found enriched in LUAD stroma compared with LUSC and mast cells were mostly present in the LUSC stroma compared with LUAD (Fig 2E). Together, these results point to a more myeloid-enriched microenvironment in LUSC compared with LUAD.

Analysis of immune cell neighborhoods (CN) revealed 7 spatial clusters based on their immune composition, with neighborhoods of a single cell type (CN7: B cell, CN4: macrophages and CN3: neutrophils), T cells (CN1 and 2 with higher prevalence of CD8 or CD4 respectively), lymphoid cells (CN6: B and T cells) and a mix of myeloid and T cells (CN5: T cells with macrophages and mast cells) (Fig 2F). Evaluating the presence of these clusters in LUAD and LUSC, we observed B cell-enriched CN7 in the stroma and at the border of LUAD, whereas neutrophil-enriched CN3 was present in the stroma of LUSC (Fig 2G) indicating that these enriched cell populations observed in each tumor subtypes infiltrate the tumor as cell communities and not as individual cells. Interestingly the myeloid/T cell cluster was enriched in the stroma of LUSC compared with LUAD (Fig 2G).
Together, these analyses revealed key differences in the spatial organisation and composition of the TME in LUSC and LUAD, highlighting essential immune cell communities characteristic of each tumor type.

Neutrophil infiltration is associated with worse patient outcomes and type I interferon signaling in LUAD

We then investigated the heterogeneity of the TME between individual tumors in LUAD and LUSC samples. Quantification of the proportions of lymphoid and myeloid cells in each sample followed by unsupervised clustering of samples resulted in the stratification of patients into 2 subgroups in LUSC and 3 subgroups in LUAD. In LUSC, 15 tumors were characterised by a mix of lymphoid and myeloid cell infiltration (LM-enriched, 75%), with a TME rich in T and B cells with macrophages, mast cells and dendritic cells. Five LUSC tumors were classified as myeloid-enriched with little lymphoid cell infiltration (M-enriched, 25%) (Fig. 3A). In LUAD, most tumors had high lymphoid infiltration (84%) either alone (L-enriched, n=21, 48%) or mixed with myeloid cell infiltration (LM-enriched, n=16, 36%) (Fig 3B). Myeloid-enriched tumors only represented 15% of the LUAD samples (M-enriched, n=7). $EGFR^{mut}$ and $KRAS^{mut}$ tumors were found in each subgroup with one $EGFR^{L858R}$ in each group, 5 $KRAS^{G12C}$ and 1 $KRAS^{G12D}$ in the 21 L-enriched tumors (28.5%), 2 $KRAS^{G12C}$ and 1 $KRAS^{G12V}$ in the 16 LM-enriched (18.7%), 1 $KRAS^{G12C}$ and 1 $KRAS^{G12A}$ in the 7 M-enriched (28.5%) tumors (Fig. 3B).

In both LUAD and LUSC, LM and L-enriched tumors had high proportions of T, B or NK cells, although high B or T cell infiltration appeared to be mostly mutually exclusive (Fig. 3A and B). In M-enriched tumors, each myeloid cell subtype was located equally in the different tumor compartments with the exception of dendritic cells that were more often found at the tumor border or in the stroma in LUAD. The expression of functional markers of myeloid cells in LUAD was similar in each individual compartment. Strikingly, the myeloid infiltrate in LM-enriched tumors was distinct from M-enriched tumors, where LM-enriched tumors had high infiltration of macrophages but low neutrophil infiltration. In contrast, the TME of M-enriched tumors was predominantly composed of neutrophils. Cell neighborhood analysis revealed that in all compartments of M-enriched tumors, neutrophils were present in clusters compared with L- and LM-enriched tumors (Fig 3C, 3D).

Patients with M-enriched tumors were found to have worse overall survival, irrespective of histological subtypes. Relapse-free survival (RFS) data were not available for most LUSC patients, hence we focused on LUAD patients to investigate the association between immune infiltration, RFS and gene expression profile. Six out of the seven patients with an M-enriched LUAD had an RFS of less than 10 months, significantly shorter than patients with L and LM-enriched LUAD (median RFS 20.7 months and 40.9 months, respectively, Fig 3E). Of note,

the long survivor with an M-enriched tumor had an *EGFR*^{L858R} mutation characterised by a distinct TME compared with the other M-enriched tumors, with enrichment in mast cells and low levels of neutrophil infiltration. This observation is consistent with previous results showing that increased mast cells in the TME are associated with never-smoker patients and prolonged survival[13]. We then combined all patients with tumors with lymphoid infiltration (L-enriched and LM-enriched) as the LLM-enriched subgroup for further analysis. Only when quantifying immune cell infiltration in the different compartments did we observe that a tumor core infiltrated with B cells was significantly associated with long RFS, consistent with previous work describing B cells infiltration as a predictor of long survival[13].

We then compared the transcriptomic profile of panCK^{+} tumor cells in M-enriched vs LLM-enriched LUAD. We observed an upregulation of genes associated with type I IFN signaling in M-enriched tumors (*IFNAR2*, *LY6E*, *IFI27*, *IFI44*, *IF44L*, *IFI6*, *XAF1*, *MX1*, *ISG15*) compared with LLM tumors (Fig 3F). Chronic exposure to type I IFN can induce myeloid cell recruitment and promote an immunosuppressive phenotype, dampening anti-tumor immune response[25]. Type I IFN signaling has also been shown to activate neutrophils with a pro-tumorigenic phenotype[25–27] suggesting cancer cells in M-enriched tumor may support the recruitment and activation of myeloid cells. In contrast, genes associated with angiogenesis (*VEGFA*), lymphoid cell recruitment and activation (*BSG*, *DOCK5*) and the formation of tertiary lymphoid structure (*LTBR*)[28] were downregulated in M-enriched tumors.

Overall, these results demonstrate the inter-tumor heterogeneity in the TME of NSCLC, enabling the stratification of patients according to different types of immune infiltrate. We identified a subset of M-enriched tumors with a TME rich in neutrophils that was not observed when lymphoid cells were also present in the TME. Patients with these distinct M-enriched tumors had worse clinical outcomes, whereas LLM-enriched tumor with B cell infiltration specifically in the tumor core had better RFS. In addition, the integration of tumor cell transcriptomic data suggested that tumor cell phenotypes driven by type I IFN signals dictate the composition of the TME in LUAD and that neutrophils may further reinforce this phenotype to promote a pro-tumorigenic environment, resulting in short RFS.

CD14^{+}CD4^{+} and CD14^{+}CD8^{+} T cells are present in the microenvironment of LUAD and LUSC tumors

We then evaluated whether CD14^{+} T cells were also a feature of NSCLC, as described in hepatocarcinoma[17]. Quantification of CD14 expression in immune cell subsets in LUAD and

LUSC tumors revealed that a subset of T cells expressed CD14 (Fig 4A and 4B), the co-receptor for TLR-4–mediated LPS recognition usually expressed by myeloid cells, indicating that these cells may be present in more organs than the liver, skin and lymph node as described previously[17]. $CD14^+CD4^+$ T cells were detected at a higher frequency than $CD14^+CD8^+$ T cells in both LUAD and LUSC, contrary to the results described in the liver[17]. $CD14^+$ lymphoid cells represented 3 to 12% of NK, $CD8^+$ and $CD4^+$ T cells in LUAD and 12 to 18 % of these cellular subsets in LUSC (Fig 4C). As a proportion of their parent population, $CD14^+CD4^+$ T cells were present equally in the tumor core, at the border or stroma. The presence of $CD14^+$ T cells in NSCLC was further confirmed by flow cytometry analysis of fresh human lung tumors (Fig 4D). Image cytometry and Hoechst 33342 analysis confirmed that $CD14^+CD4^+$ T cells were single cells and not a complex of monocytes/T cells as detected in the blood[29,30] (Fig 4E). In LUAD, $CD14^+CD4^+$ T cells were enriched in all CN clusters where T cells are present (CN1, 2, 5 and 6) indicating no particular tropism of these cells to a specific cellular community (Fig 4F). In LUSC, $CD14^+$ T cells were mostly present in the T cells cluster enriched for $CD4^+$ T cells (CN2).

Overall, these data reveal the existence of a discrete subset of $CD4^+$ and $CD8^+$ T cells expressing the myeloid marker CD14 in NSCLC.

$CD14^+$ T cells are clonally expanded effector T cells and are associated with better overall survival in LUAD

Functional characterisation of $CD14^+CD4^+$ and $CD14^+CD8^+$ T cells based on spatial proteomics data revealed $CD14^+CD4^+$ T cells express other prototypic markers of myeloid cells (MHC-II, CD16, CD163, CD206), and a marker of tissue residency (CD49a) (Fig 5A). Flow cytometry data further showed that $CD14^+CD4^+$ T cells express higher levels of Ki67, IFNγ, and CTLA4, and lower levels of PD1 and ICOS than $CD14^-CD4^+$ T cells, suggesting $CD14^+CD4^+$ T cells have a more active effector phenotype than their $CD14^-$ counterparts (Fig 5B). $CD14^+CD4^+$ T cells were almost consistently expressing CD39, a marker of tumor-specific lymphocytes[31], whereas only a subset of $CD14^-CD4^+$ T cells expressed CD39, suggesting that $CD14^+CD4^+$ T cells are enriched for tumor-specific T cell clones (Fig 5C). To assess the clonality of $CD14^+$ T cells, we compared the TCRβ repertoire of $CD14^+CD4^+$ and $CD14^-CD4^+$ T cells by TCR sequencing of sorted cell subsets. Sequencing results showed an expansion of TCRβ clones in $CD14^+$ cells compared to $CD14^-$ cells, indicating $CD14^+CD4^+$ T cells are an expanded population of T cell clones present in tumors (Fig 5D).

Strikingly, LUAD LLM tumors with high infiltration of $CD14^+CD4^+$ T or $CD14^+CD8^+$ T cells in the tumor core had a better overall survival (Fig 5E) than tumors with little infiltration of $CD14^+CD4^+/CD8^+$ T cells, suggesting that $CD14^+$ T cells, that have a more effector phenotype than $CD14^-$ cells, may better facilitate anti-tumor immunity than $CD14^-$ T cells. We then evaluated the transcriptomic profile of LUAD LLM tumors with high $CD14^+CD4^+$ T cells infiltration. KEGG pathway analysis revealed that pathways associated cytokine signaling were enriched in tumors with high $CD14^+CD4^+$ T cells infiltration compared with tumors with low $CD14^+CD4^+$ T cells infiltration. On the other hand, metabolic pathways were downregulated in tumors with high infiltration of $CD14^+CD4^+$ T cells (Fig 5F). Tumors with $CD14^+CD8^+$ T cell infiltration display enrichment for gene expression in similar pathway. Gene set enrichment analysis (GSEA) further demonstrated that tumors with high $CD14^+CD4^+$ T or $CD14^+CD8^+$ T cells expressed a strong gene signature for genes involved in TNFα signaling, a central inflammatory cytokine also involved in tumor cell apoptosis (Fig 5G).

Discussion

Advances in cancer immunotherapy have greatly improved outcomes for some lung cancer patients. However, only 20% of patients respond to treatment[32], indicating that alternative approaches to increase anti-cancer immunity are in dire need. Therapeutic approaches that would augment the recruitment of the right type of immune cells to the TME will enhance anti-tumor immunity. In-depth characterisation of the composition and spatial organisation of individual immune cells in the TME, and the signals that regulate them, is essential in identifying how to attract specific immune cells to bolster anti-tumor immunity. Here, we performed deep spatial proteomic and transcriptomic profiling of immune and tumor cells in NSCLC samples. We identified neutrophil communities present at the border of the tumor front, maintained by type I IFN signaling, are associated with short-term patient survival in LUAD and LUSC. Importantly, we show that myeloid-instructed $CD14^+$ T cells infiltrating the tumor core are associated with long-term patient survival in LUAD. Tumors with high $CD14^+$ T cell infiltration have a transcriptomic profile enriched in cytokine signaling that may facilitate the recruitment or reprogramming of these cells.

In situ analysis of individual cells in solid tumors presents a clear advantage over single cell analysis of dissociated tissue. Notably, the architecture of the tissue is preserved, adding to the depth of knowledge on the role of cell communities in the anti-tumor immune response. In

addition, this approach also avoids disproportionate recovery of different cell types, which is known to occur after tissue disruption. Our comparison of the *in situ* TME in different histological subtypes of NSCLC revealed similarities and distinctions in the composition and organisation of the TME of LUAD and LUSC. As described by others[11,20], we observed a higher proportion of immune cells in the stroma and at the tumor border than in the tumor core. However, macrophages and $CD8^+$ T cells were more predominant in the tumor core than the border and the stroma in both LUAD and LUSC. Myeloid cells were always observed in LUSC whereas nearly half of the LUAD samples had no to little myeloid cell infiltration. Cell neighborhood analysis showed that immune cells were mostly present as clusters of single cell types or cells from similar lineages. Mixed myeloid and T-cell cellular neighborhoods were a distinctive feature of the LUSC TME, whereas B-cell clusters were only observed in LUAD and associated with better survival in LUAD, as described by Sorin et al[13].

By profiling the TME in NSCLC, we were able to stratify LUAD and LUSC in different immune categories. M-enriched tumors had a distinct myeloid cell infiltration compared with LM-enriched tumors. While neutrophils were the predominant myeloid cell type in M-enriched tumors, macrophages constituted the bulk of the myeloid infiltrate in LM-enriched tumors. Neutrophils have a multi-faceted role in cancer[26,33] but have often been associated with worse clinical outcomes in solid tumors, facilitating tumor cell extravasation and metastasis[34–36]. A high neutrophil-to-lymphocyte ratio has been associated with worse overall survival in many solid malignancies, including lung cancer[37], consistent with our observation that tumors with clusters of neutrophils had worse survival. Neutrophil activation and the formation of neutrophil extracellular traps (NETs) have been associated with rapid disease progression in lung cancer[38]. In tuberculosis (TB), type I IFN induces NETosis, exacerbating disease severity in mouse models of TB, and NETs are observed in necrotic lung lesions of patients with severe pulmonary TB[39]. We observed that neutrophil-enriched tumors had a characteristic molecular signature of type I IFN signaling. This increased type I IFN signaling may mediate NETosis in neutrophil-infiltrated tumors, facilitating cell metastasis and relapse of disease. Inducers of type I IFN have been proposed as possible anti-tumor therapy with mixed results in clinical trials[40,41]. Our results suggest that type I IFN-mediated therapy will need to be targeted to a subset of tumors and may not be amenable to neutrophil-infiltrated tumors. Indeed, sustained type I IFN activity has been associated with resistance to anti-PD-1 immune checkpoint blockade by reducing T cell activity in human cancers[42,43]. Inhibiting type I IFN may be a therapeutic strategy to reduce NETosis and the deleterious impact of neutrophils in neutrophil-

infiltrated NSCLC. Given the pleiotropic role of type I IFN, targeted therapy to the tumor site, with the use of bispecific antibodies such as described for ErbB2 expressing tumor cells[44], will need to be developed.

Focusing on tumors with lymphoid cell infiltration, we observed that a subset of $CD4^+$ and $CD8^+$ T cells expressed the myeloid cell marker CD14, similar to the $CD14^+CD8^+$ and $CD14^+CD4^+$ T cells described in human liver[17]. Detailed analysis by Pallett *et al.* demonstrated that $CD14^+$ T cells were myeloid-instructed T cells, in which $CD8^+$ T cells acquired cellular myeloid materials from $CD14^+$ myeloid cells in a contact-dependent manner. Exposure to bacterial LPS promoted the transfer of myeloid materials to T cells, with the presence of bacteria reshaping the local immunity and inducing the expansion of $CD14^+CD8^+$ T cells[17]. The lung is host to a diverse range of commensal bacteria[45] and increased bacterial colonisation is observed in lung tumors[46–49]. Further studies would be required to investigate the relationship between $CD14^+$ T cells, the tumor microbiota and the implication for response to immunotherapy. Importantly, we observed that patients with tumors with a high infiltration of $CD14^+$ expressing $CD4^+$ T cells had prolonged survival, pointing to $CD14^+CD4^+$ T cells being important mediators of anti-tumor immunity. $CD14^+CD4^+$ T cells were more frequent than $CD14^+CD8^+$ T cells and had a more effector phenotype than their $CD14^-$ counterparts. $CD14^+$ T cells were clonally expanded and expressed the tumor-specific marker of tumor infiltrating lymphocyte CD39[31], suggesting that $CD14^+CD4^+$ T cells represent a pool of activated tumor-specific T cell clones. GSEA showed that tumor cells growing in a $CD14^+CD4^+$ TME had a strong signature for genes in the cytokine signaling pathway, including TNFα. Whether TNFα supports the reprogramming or recruitment of myeloid-instructed $CD14^+$ T cells or $CD14^+$ T cells stimulated TNFα signaling in tumor cells remains to be determined. Nevertheless, factors that could promote the reprogramming of adaptive immune cells towards this myeloid-instructed phenotype may constitute a novel approach to increase anti-tumor immunity.

Overall, our study demonstrates the importance of undertaking a comprehensive analysis of the tumour ecosystem with hi-plex in situ molecular approaches to uncover novel cell types and decipher spatial relationships between immune and tumour cells. Our approach revealed how myeloid-instructed T cells in the TME may participate in tumor immune surveillance. Targeting the recruitment or reprogramming of myeloid-instructed T cells to the tumor core may provide novel therapeutic avenues for lung cancer patients.

Methods

Human NSCLC cohort

Written informed consent was obtained from all patients by the Victorian Cancer Biobank prior to inclusion in the study, according to protocols approved by the WEHI Human Research Ethics Committee (HREC, 10/04LR). Human tonsil FFPE tissues were obtained were used for antibody validations. NSCLC specimens and associated clinical data were obtained from the Victorian Cancer Biobank from treatment-naïve, surgically resected early-stage lung cancer patients (Stage I to IIIa). Patients were classified as ever-smokers (current and ex-smokers who had quit smoking at least 1 year prior to sample collection) or never-smokers (lifetime smoking of less than 100 cigarettes). Only patients with an overall survival (OS) of less than 3 years post-surgery and with OS of more than 6 years post-surgery were included in the study. Three formalin-fixed paraffin-embedded (FFPE) serial sections (4µm thickness) were cut for H&E staining, MIBI proteomic experiment on gold-coated slides (Ionpath #567001), and for GeoMX transcriptomic experiment.

Validation of 38-plex antibody panel for MIBI

Rare earth polymer conjugated antibodies were purchased from Ionpath or conjugated to metal polymers according to manufacturer protocol (Ionpath). Briefly, 100µg of carrier-free antibody was reduced with 4mM TCEP. Partially reduced antibody was then incubated at 37°C for 1hr with the metal-loaded polymer. The antibody concentration was quantified by measuring the IgG absorbance at 280nm on the NanoDrop. The conjugated antibody was eluted to obtain a final concentration of 0.5mg/ml. All antibodies were first validated by immunohistochemistry on NSCLC tissue sections. Panels of conjugated antibodies were then evaluated on human tonsils to ensure specificity and the absence of isobaric and isotopic overlap. Antibodies were then titrated on lung cancer tissues before being pooled in a 38-plex panel for staining of the complete cohort.

Slide staining and scanning on MIBI

Slides were processed as per manufacturer protocol and stained with our bespoke 38-plex antibody panel. Briefly, antigen retrieval was performed with Tris EDTA pH9 (Agilent, #S236784-2) using the PT Link Module (Thermo Scientific), sections blocked with 10% donkey serum and stained overnight with 36 conjugated antibodies. Slides were then washed

in TBS-0.1% Tween and stained for 30 min with 2 antibodies before being dehydrated and post-fixed with 2% glutaraldehyde. Slides were stored in a vacuum chamber before scanning. Fields of view of 400x400µm (1024x1024 pixels) were acquired at a dwell time of 1ms. The mass-spec pixel data generated is automatically converted into TIFF images. MIBI images were pre-processed for isobaric correction using MIBI/O (Ionapth) and visualised on QuPath[18]. Adjacent FOVs were stitched together using a groovy script plugin in QuPath[50].

Single-cell segmentation

Cell segmentation was performed using a QuPath extension applying Mesmer[19,51]. The dsDNA channel was used as the nuclei features and the matrix addition of the median normalised MHC I channel and the panCK channel was used as the membrane features. Segmented cells with a nuclei area of <50 pixels and cells touching the border of images were removed.

Single-cell phenotyping

Cell classification was performed using the supervised method XGBoost. We manually annotated 52,719 cells using in-house developed tools on QuPath. Cells were annotated as epithelial cells, stromal cells, B cells, $CD4^+$ T cells, $CD8^+$ T cells, Treg cells, NK cells, $\gamma\delta$T cells, macrophages, dendritic cells, neutrophils, mast cells, or others. Annotations were assigned to cells based on the shape and intensity of the markers within the cell boundaries visible on the images. All markers were used to train the model. Each marker was measured in four compartments: nucleus, cytoplasm, membrane, and the entire cell. In each cell compartment, the measurements calculated were mean, standard deviation, and the 0.7, 0.8, 0.9, 0.95, 0.96, 0.97, 0.98, 0.99, 0.995, 0.999 quantiles. A polynomial feature generation of degree two was used between markers expected to be co-expressed. The combinations were generated from pools of markers expected to be co-expressed. These features were generated on cell mean measurements of the markers. In total 1713 features were used to train the model. To compensate for the imbalanced data, we used the synthetic minority oversampling technique (SMOTE). To select the hyper-parameters, we used the Bayesian search cross validation (https://scikit-optimize.github.io/stable/modules/generated/skopt.BayesSearchCV.html). In assessing the results of the training confusion matrices, scores such as f1, balanced accuracy, ROC AUC score, were used.

Tissue compartment classification immune subgroups

Twelve different pixel classifiers were trained in QuPath and applied to our cohort of 64 patients to delimit the tumor and stroma area. For spatial analysis, three compartments were created: tumor core, border and stroma where the border was defined as 40µm inside and outside the tumor area. Patients were grouped into myeloid-, lymphoid-myeloid- or lymphoid-enriched (M-, LM-, L-enriched) after an unsupervised clustering of the proportions of lymphoid and myeloid cells in each sample.

Cell neighborhood clustering

Cell neighborhood (CN) clusters were defined by first determining the 10 closest neighbours (excluding itself) of every cell. The cell type frequencies were determined and converted into proportions. These proportions were used in a K means clustering with k=7. Cell type proportions have been z-score normalised within each cluster.

Statistical analysis

Statistical analyses were performed using R (2023.06.1+524). Boxplots present median +/- standard deviation. Non-normal data were compared between two groups using Wilcoxon rank sum test. Samples with less than 5 cells of the cell type of interest were excluded from the analysis. The significance between two groups in Kaplan Meier survival curves was calculated using log-rank (Mantel-Cox) test. In the heatmaps, percentages are calculated for each patient and then z-score normalised across all patients using the scale function with default parameters in R.

Human lung and tumor tissue dissociation

Lung and tumor samples were either processed immediately or held intact for a maximum of 16 h at 4°C in DMEM/F12 media (Gibco) supplemented with 1 mg/mL of penicillin and streptomycin (Invitrogen). Surgical samples were minced then digested for 1 h at 37°C with 2 mg/mL collagenase I (Worthington, #LS004197) and 200 U/mL deoxyribonuclease (Worthington, #LS002140) in 0.2% D-glucose (Sigma) in DPBS (Gibco), as previously described[3]. The cell suspension was filtered through 100 µm strainer (Falcon) and washed with 2% FCS-PBS, followed by red blood cell lysis and further washing with 2% FCS-PBS to obtain a single cell suspension. Single cell suspensions were either stained immediately for flow cytometry analysis or cryopreserved in 90% FCS:10% DMSO and stored in liquid nitrogen prior to staining.

Flow cytometry

Cells were stained with fixable viability dye Zombie NIR (Biolegend) for 15 min. Cells were washed with 2%FCS-PBS, then blocked with anti-CD16/32 FCRγ antibody (WEHI antibody facility) for 10 min. Cells were stained with extracellullar antibodies for 30 min at 4°C. Cells were then fixed and permeabilised with Foxp3/Transcription Factor Staining Kit (eBiosciences) and stained with intracellular antibodies for 30 min at 4°C. Samples were resuspended in FACS buffer (2% FCS in PBS) and data acquired using an Aurora spectral unmixing cytometer (CyTEK). Interrogation of singlet and doublet cells was performed by staining cells with extracellular antibodies for 30 mins 4°C then incubated with Hoechst 33342 (5µg/ml) for 30min at ˚C. Samples were acquired using a BD Symphony flow cytometer. Data were analysed using FlowJo (Tree Star).

Image Cytometry

Real time images were captured using BD FACSDiscover™ S8 Cell Sorter running BD FACSChorus™ acquisition software (BD Biosciences, San Jose). The instrument contains 5 lasers with 6 spatially separated laser intercepts (the blue laser is split to support full-spectrum detection at one intercept and BD CellView™ imaging detection at a second intercept. Live cells were gated on CD45-PE^{+}CD3-BV570^{+}CD4-RB545^{+}. The images for each cell were captured in real-time with the following detectors and bandpass filters, light-loss, forward scatter, side scatter (488/15), Image Channel 1 (534/46, CD4), and image channel 3 (788/225, CD14). Co-localization of CD4 and CD14 were determined using the imaging data and the following image analysis, Max Intensity (CD14 BB700) vs Correlation (CD4 RB545/CD14 BB700) plot.

TCR sequencing

CD45^{+}CD3^{+}CD4^{+} CD14^{+}or CD14^{-} T cells were sorted on the Aria Fusion (BD) and DNA extracted using DNeasy Blood & Tissue kit (Qiagen). DNA Integrity was measured on the Tapestation 4200 (Agilent). Samples with a DNA Integrity Number > 8.5 were sent for TCRβ sequencing by ImmunoSeq (Adaptive Biotechnologies, Seattle). TCR reads and sequences were analysed on the Immunoseq data analysis platform (Adaptive Biotechnologies).

GeoMx data collection

FFPE sections from 64 NSCLC samples were sent to the NanoString Centre of Excellence in Spatial Biology (Griffith University) for sample processing and data collection on the GeoMx

platform (Nanostring). Slides were baked at 60°C for 90 min. and deparaffinised at 72°C for 30min, Heat-induced epitope retrieval for 20 min and Proteinase K treatment (1µg/mL) for 15 min using the automated LEICA BOND Rx system. Immunofluorescent staining was performed using the morphology antibodies from Nanostring Solid Tumor Morphology kit: SYTO13 (nucleus, 1:10 dilution), PanCK-AF532 (tumor cells, 1:40 dilution) and CD45-AF594 (immune cells, 1:40 dilution). For in-situ hybridisation for next generation sequencing, tissue sections were then hybridized with Whole Transcriptome Atlas (WTA; Lot# HWTA21003) probes for 16 hours at 37°C in a humidity-controlled chamber. Two segments were collected: PanCK positive cells and CD45 positive cells, with a minimum of 200 cells collected for each individual area of illumination (AOI). A total of 345 AOIs were collected.

GeoMx data analysis

NanoString GeoMx DSP data was processed with GeoMx DSP Data Analysis Suite (https://nanostring.com/products/geomx-digital-spatial-profiler/geoscript-hub/). All downstream analysis was performed in the R statistical programming language (version 4.3.2) using predominantly Bioconductor packages (version 3.18). Further quality control was performed using the **standR** Bioconductor R package version 1.6[52]. Library sizes were normalized with the TMM method[53], as implemented in the *geomxNorm* function of the **standR** package. Count data were transformed to log2-counts per million, voom precision weights were estimated and linear models for differential expression analysis were fitted using **edgeR**'s *voomLmFit* function with additional cyclicloess normalization (**edgeR** version 4.0)[54,55]. For the comparison of LAUD and LUSC cancer types, age and sex were included as covariates in the linear model. Differential expression was assessed using moderated t-statistics[56] with robust empirical Bayes variance estimation[57]. Genes with a false discovery rate < 0.05 and log-fold-change threshold > 1.1 were defined as significantly differentially expressed using TREAT[58,59]. For LUAD M vs LLM comparison, the cancer sub-types, age and smoking status were included in the linear model. Genes were ranked using p-values obtained from moderated t-statistics. The top ranked genes with a log-fold change < -0.5 and > 0.5 are highlighted in the mean-difference plot. For the comparison of $CD14^{+}$-high vs $CD14^{+}$-low tumours, CD14 status was included in the linear model together with smoking status. CD14 status was determined as high/low using the MIBI data and defined as areas of illumination (AOI) with greater/smaller percentage of CD14 positive cells than the median value across all AOI. Gene set testing to test for enrichment of REACTOME gene sets, Gene Ontology terms,

KEGG pathways and Hallmark gene sets from the Molecular Signatures Database (MSigDB)[60] was performed using the *camera* function in **limma** Bioconductor R package (version 3.58)[61,62]. For Fig 5G, Fig 3F, genes from selected pathways were highlighted using barcode plots, where the x-axis represents ordered moderated t-statistics from the testing procedure described above. Significant differences in proportions of cells with higher expression of functional markers between $CD14^+$ and $CD14^-$ were assessed using a *propeller* test from the **speckle** Bioconductor R package (version 1.2)[63].

Data Availability

The sequence data generated in this study are publicly available in Gene Expression Omnibus (GEO) at GSEXXXX (TBC) and within the article. Codes are available at https://github.com/WEHI-labatlab/

Acknowledgements

We thank WEHI facilities including Histology (Emma Pan and Ellen Tsui) and Flow cytometry (Simon Monard) for expert advice and performing experiments. We are grateful to the Victorian Cancer Biobank and all lung cancer patients who participated in this study. Real time images of the cells were captured using a BD FACSDiscover™ S8 Cell Sorter located at BD Melbourne, Australia with the assistance of the BD Biosciences ANZ applications team. The MIBI studies were supported by the Australian Cancer Research Foundation Program for Resolving Cancer Complexity and Therapeutic Resistance. C.M. was supported by funds from the Ireland Trust Bequest and the Harry Secomb Trust - Perpetual Impact. B.P. is supported by an NHMRC Investigator Grant (GNT1175653). M.L.A.L. is supported by funding from the Viertel Foundation Senior Medical Research Fellowship. This work is supported by a NHMRC Ideas Grant (GNT1182155), the Jenny Tatchell Fund and by funds from the Operational Infrastructure Support Program provided by the Victorian Government and NHMRC IRIISS (Independent Research Institutes Infrastructure Support Scheme) Grant.

Declaration of interests

The authors declare no competing interests.

Figure Legends

Figure 1: Spatial analysis of the tumor microenvironment and tumor cells in human non-small cell lung cancer samples. **A.** Top: Kaplan Meier survival curve showing overall survival of resected non-small cell lung cancer (NSCLC) sample cohort. Samples from patient with overall survival (OS) less than 3 years or more than 6 years were selected for this study. Bottom: Donuts graph representing the characteristics of the lung adenocarcinoma (LUAD) and squamous cell carcinoma (LUSC) patients analysed. The numbers represent the final sample size of patients profiled. Layers are unrelated. G: grade; NC: not cited. **B.** Overview of the workflow for the spatial analysis. Regions of interest (ROI) were selected by a pathologist based on H&E stain. Adjacent slides were used for spatial proteomic (MIBI) and spatial transcriptomic (Nanostring GeoMx). For GeoMx analysis, selection of areas of illumination (AOI) was based on the protein expression of CD45 (pink) and cytokeratin (panCK, green). Scale bar: 50µm. For MIBI scanning, coordinates of a selected ROI were transposed to the antibody-stained slide and scanned. Scale bar: 50µm. **C.** Heatmap depicting the mean expression of each marker (or column) z-score normalised across all the cell types (rows) identified by the XGBoost model. Right panel shows the number of cells in each category. **D.** UMAP of immune cell types generated in all samples using the mean intensity measurement of each phenotypic marker in all immune cells. The colors reflect the phenotype assigned by the XGBoost model.

Figure 2. Cell communities containing myeloid cells are a feature of the LUSC TME. **A.** Heatmap showing the expression of the top 50 differentially expressed genes in cytokeratin positive tumor cells (panCK$^+$ AOI, GeoMx) between LUAD and LUSC. Data show z-scores. **B.** Top: Heatmap depicting the proportion of MHC I$^+$, MHC II$^+$, IFNγ$^+$, and Ki67$^+$ in tumor cells (PanCK$^+$) in individual patient samples from MIBI analysis (z-score, scaled across all patients). Samples ordered highest to lowest relative proportion of MHC I$^+$ cells. Middle: heatmap representing the proportion of immune cell infiltration in the three tissue compartments (tumor core, border, stroma) in individual patients (z-score, scaled across all patients). Bottom: Clinical and molecular data on individual patients. OS: overall survival. **C.** Proportion of the different immune cell types in LUAD and LUSC, as determined by MIBI. Data show median ± SD. n=44 LUAD, n=20 LUSC. **D.** Boxplots showing the localisation of CD4$^+$ T cells and CD8$^+$ T cells in the different spatial tissue compartments in LUAD and LUSC patients. Data show median ± SD. ****, $p<0.0001$; ***, $p<0.001$; **, $p<0.01$; *, $p<0.05$

comparing the different compartments, Wilcoxon test. n=44 LUAD, n=20 LUSC. **E.** Volcano plots comparing the proportion of each immune cell subtypes in the three compartments in LUAD and LUSC samples. Significant -log10(p-value) is indicated by horizontal dash line, Wilcoxon test. n=44 LUAD, n=20 LUSC. **F.** Heatmap showing seven cell neighborhoods (CN) detected in NSCLC samples, and the cell type composition for each cluster. Right panel: representative images showing rendering of different CN in tumor core (grey), border (blue) and stroma (dark grey). Scale bar: 50µm. **G.** Volcano plots comparing the proportion of each CN cluster in the three compartments between LUAD and LUSC samples. Significant -log10(p-value) is indicated by horizontal dash line, Wilcoxon test.

Figure 3. Enrichment for neutrophil clusters is associated with worst relapse-free survival in LUAD patients. **A and B.** Heatmap showing the z-score scaled by column of the proportion of each immune cell subtype in all immune cells in individual samples in LUAD and LUSC. Hierarchical clustering stratified the TME in LUSC patients as lymphoid/myeloid-enriched (LM-enriched, n=15) or myeloid-enriched (M-enriched, n=5) (**A**). LUAD patients were stratified as lymphoid-enriched (L-enriched, n=21), lymphoid/myeloid-enriched (LM-enriched, n=16) or myeloid-enriched (M-enriched, n=7). KRAS and EGFR mutations are specified at the bottom of LUAD patients. '-': not available. (**B**). **C.** Representative image showing clustering of neutrophils in a LUAD tumor (MH1041). Scale bar: 50µm. **D.** Volcano plots comparing the proportion of each CN cluster in the three compartments between M- and L+LM-enriched LUAD samples. **E.** Kaplan-Meier survival curve showing relapse-free survival in the three groups of LUAD patients. *, $p<0.05$, log-rank (Mantel-Cox) test. L-enriched, n=21; LM-enriched, n=16; M-enriched, n=7. **F**. Gene set enrichment analysis showing enrichment for indicated GO terms between M- and LLM-enriched LUAD samples.

Figure 4. Myeloid-instructed CD14$^+$ T cells infiltrate tumors in non-small cell lung cancer. **A.** Proportion of immune cell types expressing CD14 in LUAD and LUSC as determined by MIBI. Data show median ± SD. n=44 LUAD, n=20 LUSC. **B.** Representative MIBI images showing the expression of CD14, CD3, CD8 and CD4 in LUAD tumor (AH0353). Arrow shows CD14 expression in CD3$^+$CD4$^+$ or CD3$^+$CD8$^+$ T cells. Scale bar: 50µm. **C.** Box plot showing the proportion of lymphoid cell subsets expressing CD14 in LUAD and LUSC as determined by MIBI. Data show median ± SD. **, $p<0.01$; *, $p<0.05$, Wilcoxon test. n=42 LUAD, n=20 LUSC. **D.** Representative flow cytometry plot showing CD14 expression in

$CD4^+$ T cells gated on $CD45^+CD3^+$ cells in a LUAD (MH0069). **E.** Representative image cytometry images showing the expression of CD14 and CD4 on $CD45^+CD3^+CD4^+$ cells. n=2. **F.** Box plots showing the proportion of $CD14^+CD4^+$ or $CD14^+CD8^+$ T cells in each cell neighborhood (CN) in LUAD samples (n=42). Data show median ± SD.

Figure 5. Infiltration of $CD14^+CD4^+$ T cells is associated with better overall survival in LUAD patients. **A.** Expression of MHC-II, CD16, CD163, CD206 and CD49a in $CD14^+CD4^+$, $CD14^-CD4^+$ T cells as determined by MIBI. *, p<0.05, paired t-test. Data show median ± SD. n=42 LUAD. **B.** Mean fluorescence intensity (MFI) of myeloid (MHC-II) and functional markers (Ki67, IFNγ, CTLA4) in $CD14^+CD4^+$ and $CD14^-CD4^+$ T cells in NSCLC as assessed by flow cytometry. Top panel show representative FACS image for each marker. Cells were gated on Live $CD45^+CD3^+CD4^+CD14^{+/-}$ cells. n=4 LUAD, n=3 LUSC and n=1 carcinoid. **, p<0.01; *, p<0.05, paired t-test between $CD14^+$ and $CD14^-$ T cell subsets. **C.** Proportion of $CD14^+CD4^+$ and $CD14^-CD4^+$ T cells expressing CD39. n=4 LUAD, n=3 LUSC and n=1 carcinoid. ***, p<0.001, **, p<0.01; *, p<0.05, paired t-test between $CD14^+$ and $CD14^-$ T cell subsets. **D.** Frequency of the productive TCR sequences (top 20) in paired $CD14^+CD4^+$ and $CD14^-CD4^+$ T cells. n=2 LUAD and n=2 LUSC. Right panel shows frequency of the top 20 productive TCR sequences in $CD14^+CD4^+$ and $CD14^-CD4^+$ T cells from a LUAD (MH0059) and a LUSC sample (MH0061). **E.** Kaplan-Meier survival curve showing overall survival of LLM-enriched LUAD patients with low or high $CD14^+CD4^+/CD8^+$ infiltration in the tumor core. The cut off used to separate low and high expression is the mean. n=12 low $CD14^+CD4^+/CD8^+$-infiltrated tumours; n=4 high $CD14^+CD4^+/CD8^+$-infiltrated tumours. *, p<0.05; log-rank (Mantel-Cox) test. **F.** KEGG pathway analysis showing selected pathways with FDR< 0.05. n=6 low $CD14^+CD4^+$-infiltrated tumours; n=3 high $CD14^+CD4^+$-infiltrated tumours. **G.** Barcode plot showing gene set enrichment analysis in GeoMx data from $panCK^+$ cells comparing tumors with high $CD14^+CD4^+$ T cells infiltration with tumors with low $CD14^+CD4^+$ T cells infiltration as determined by MIBI.

References

1. Rizvi, H., Sanchez-Vega, F., La, K., Chatila, W., Jonsson, P., Halpenny, D., Plodkowski, A., Long, N., Sauter, J.L., Rekhtman, N., et al. (2018). Molecular Determinants of Response to Anti–Programmed Cell Death (PD)-1 and Anti–Programmed Death-Ligand 1 (PD-L1) Blockade in Patients With Non–Small-Cell Lung Cancer Profiled With Targeted Next-Generation Sequencing. JCO *36*, 633–641. 10.1200/jco.2017.75.3384.

2. Hellmann, M.D., Nathanson, T., Rizvi, H., Creelan, B.C., Sanchez-Vega, F., Ahuja, A., Ni, A., Novik, J.B., Mangarin, L.M.B., Abu-Akeel, M., et al. (2018). Genomic Features of Response to Combination Immunotherapy in Patients with Advanced Non- Small-Cell Lung Cancer. Cancer Cell *33*, 843-852.e4. 10.1016/j.ccell.2018.03.018.

3. Weeden, C.E., Gayevskiy, V., Marceaux, C., Batey, D., Tan, T., Yokote, K., Ribera, N.T., Clatch, A., Christo, S., Teh, C.E., et al. (2023). Early immune pressure initiated by tissue-resident memory T cells sculpts tumor evolution in non-small cell lung cancer. Cancer Cell. 10.1016/j.ccell.2023.03.019.

4. Angelova, M., Mlecnik, B., Vasaturo, A., Bindea, G., Fredriksen, T., Lafontaine, L., Buttard, B., Morgand, E., Bruni, D., Jouret-Mourin, A., et al. (2018). Evolution of Metastases in Space and Time under Immune Selection. Cell *175*, 751-765.e16. 10.1016/j.cell.2018.09.018.

5. Kirchhammer, N., Trefny, M.P., Maur, P.A. der, Läubli, H., and Zippelius, A. (2022). Combination cancer immunotherapies: Emerging treatment strategies adapted to the tumor microenvironment. Sci Transl Med *14*, eabo3605. 10.1126/scitranslmed.abo3605.

6. Bruni, D., Angell, H.K., and Galon, J. (2020). The immune contexture and Immunoscore in cancer prognosis and therapeutic efficacy. Nat. Rev. Cancer *20*, 662–680. 10.1038/s41568-020-0285-7.

7. Borghaei, H., O'Byrne, K.J., Paz-Ares, L., Ciuleanu, T.-E., Yu, X., Pluzanski, A., Nagrial, A., Havel, L., Kowalyszyn, R.D., Valette, C.A., et al. (2023). Nivolumab plus chemotherapy in first-line metastatic non-small-cell lung cancer: results of the phase III CheckMate 227 Part 2 trial. ESMO Open *8*, 102065. 10.1016/j.esmoop.2023.102065.

8. Hellmann, M.D., Paz-Ares, L., Caro, R.B., Zurawski, B., Kim, S.-W., Costa, E.C., Park, K., Alexandru, A., Lupinacci, L., Jimenez, E. de la M., et al. (2019). Nivolumab plus Ipilimumab in Advanced Non–Small-Cell Lung Cancer. New Engl J Med *381*, 2020–2031. 10.1056/nejmoa1910231.

9. Lambrechts, D., Wauters, E., Boeckx, B., Aibar, S., Nittner, D., Burton, O., Bassez, A., Decaluwé, H., Pircher, A., Eynde, K., et al. (2018). Phenotype molding of stromal cells in the lung tumor microenvironment. Nat Med, 1–19. 10.1038/s41591-018-0096-5.

10. Guo, X., Zhang, Y., Zheng, L., Zheng, C., Song, J., Zhang, Q., Kang, B., Liu, Z., Jin, L., Xing, R., et al. (2018). Global characterization of T cells in non-small-cell lung cancer by single-cell sequencing. Nat Med, 1–17. 10.1038/s41591-018-0045-3.

11. Lavin, Y., Kobayashi, S., Leader, A., Amir, E.D., Elefant, N., Bigenwald, C., Remark, R., Sweeney, R., Becker, C.D., Levine, J.H., et al. (2017). Innate Immune Landscape in Early Lung Adenocarcinoma by Paired Single-Cell Analyses. CELL *169*, 750-757.e15. 10.1016/j.cell.2017.04.014.

12. Leader, A.M., Grout, J.A., Maier, B.B., Nabet, B.Y., Park, M.D., Tabachnikova, A., Chang, C., Walker, L., Lansky, A., Berichel, J.L., et al. (2021). Single-cell analysis of human non-small cell lung cancer lesions refines tumor classification and patient stratification. Cancer Cell, 1–29. 10.1016/j.ccell.2021.10.009.

13. Sorin, M., Rezanejad, M., Karimi, E., Fiset, B., Desharnais, L., Perus, L.J.M., Milette, S., Yu, M.W., Maritan, S.M., Doré, S., et al. (2023). Single-cell spatial landscapes of the lung tumour immune microenvironment. Nature, 1–7. 10.1038/s41586-022-05672-3.

14. Corgnac, S., Malenica, I., Mezquita, L., Auclin, E., Voilin, E., Kacher, J., Halse, H., Grynszpan, L., Signolle, N., Dayris, T., et al. (2020). CD103+CD8+ TRM Cells Accumulate in Tumors of Anti-PD-1-Responder Lung Cancer Patients and Are Tumor-Reactive Lymphocytes Enriched with Tc17. Cell Reports Medicine *1*, 100127. 10.1016/j.xcrm.2020.100127.

15. Park, S.L., Buzzai, A., Rautela, J., Hor, J.L., Hochheiser, K., Effern, M., McBain, N., Wagner, T., Edwards, J., McConville, R., et al. (2019). Tissue-resident memory CD8+ T cells promote melanoma-immune equilibrium in skin. Nature *565*, 366–371. 10.1038/s41586-018-0812-9.

16. Savas, P., Virassamy, B., Ye, C., Salim, A., Mintoff, C.P., Caramia, F., Salgado, R., Byrne, D.J., Teo, Z.L., Dushyanthen, S., et al. (2018). Single-cell profiling of breast cancer T cells reveals a tissue-resident memory subset associated with improved prognosis. Nat Med, 1–16. 10.1038/s41591-018-0078-7.

17. Pallett, L.J., Swadling, L., Diniz, M., Maini, A.A., Schwabenland, M., Gasull, A.D., Davies, J., Kucykowicz, S., Skelton, J.K., Thomas, N., et al. (2023). Tissue CD14+CD8+ T cells reprogrammed by myeloid cells and modulated by LPS. Nature *614*, 334–342. 10.1038/s41586-022-05645-6.

18. Bankhead, P., Loughrey, M.B., Fernández, J.A., Dombrowski, Y., McArt, D.G., Dunne, P.D., McQuaid, S., Gray, R.T., Murray, L.J., Coleman, H.G., et al. (2017). QuPath: Open source software for digital pathology image analysis. Sci Rep-uk *7*, 16878. 10.1038/s41598-017-17204-5.

19. Greenwald, N.F., Miller, G., Moen, E., Kong, A., Kagel, A., Dougherty, T., Fullaway, C.C., McIntosh, B.J., Leow, K.X., Schwartz, M.S., et al. (2021). Whole-cell segmentation of tissue images with human-level performance using large-scale data annotation and deep learning. Nat Biotech, 1–23. 10.1038/s41587-021-01094-0.

20. Backman, M., Strell, C., Lindberg, A., Mattsson, J.S.M., Elfving, H., Brunnström, H., O'Reilly, A., Bosic, M., Gulyas, M., Isaksson, J., et al. (2023). Spatial immunophenotyping of the tumour microenvironment in non–small cell lung cancer. Eur. J. Cancer *185*, 40–52. 10.1016/j.ejca.2023.02.012.

21. Network, T.C.G.A.R. (2014). Comprehensive molecular profiling of lung adenocarcinoma. Nature *511*, 1–9. 10.1038/nature13385.

22. Hammerman, P.S., Lawrence, M.S., Voet, D., Jing, R., Cibulskis, K., Sivachenko, A., Stojanov, P., McKenna, A., Lander, E.S., Gabriel, S., et al. (2012). Comprehensive genomic characterization of squamous cell lung cancers. Nature *489*, 519–525. 10.1038/nature11404.

23. Datar, I.J., Hauc, S.C., Desai, S., Gianino, N., Henick, B., Liu, Y., Syrigos, K., Rimm, D.L., Kavathas, P., Ferrone, S., et al. (2021). Spatial Analysis and Clinical Significance of HLA Class-I and Class-II Subunit Expression in Non-Small Cell Lung Cancer. Clinical Cancer Research *27*, 2837–2847. 10.1158/1078-0432.ccr-20-3655.

24. Montesion, M., Murugesan, K., Jin, D.X., Sharaf, R., Sanchez, N., Guria, A., Minker, M., Li, G., Fisher, V., Sokol, E.S., et al. (2021). Somatic HLA Class I Loss Is a Widespread Mechanism of Immune Evasion Which Refines the Use of Tumor Mutational Burden as a Biomarker of Checkpoint Inhibitor Response. Cancer Discov *11*, 282–292. 10.1158/2159-8290.cd-20-0672.

25. Boukhaled, G.M., Harding, S., and Brooks, D.G. (2020). Opposing Roles of Type I Interferons in Cancer Immunity. Annu. Rev. Pathol.: Mech. Dis. *16*, 1–32. 10.1146/annurev-pathol-031920-093932.

26. Quail, D.F., Amulic, B., Aziz, M., Barnes, B.J., Eruslanov, E., Fridlender, Z.G., Goodridge, H.S., Granot, Z., Hidalgo, A., Huttenlocher, A., et al. (2022). Neutrophil phenotypes and functions in cancer: A consensus statement. J. Exp. Med. *219*, e20220011. 10.1084/jem.20220011.

27. Holicek, P., Guilbaud, E., Klapp, V., Truxova, I., Spisek, R., Galluzzi, L., and Fucikova, J. (2023). Type I interferon and cancer. Immunol. Rev. 10.1111/imr.13272.
28. Drayton, D.L., Liao, S., Mounzer, R.H., and Ruddle, N.H. (2006). Lymphoid organ development: from ontogeny to neogenesis. Nat. Immunol. *7*, 344–353. 10.1038/ni1330.
29. Burel, J.G., Pomaznoy, M., Arlehamn, C.S.L., Weiskopf, D., Antunes, R. da S., Jung, Y., Babor, M., Schulten, V., Seumois, G., Greenbaum, J.A., et al. (2019). Circulating T cell-monocyte complexes are markers of immune perturbations. eLife *8*, e46045. 10.7554/elife.46045.
30. Burel, J.G., Pomaznoy, M., Arlehamn, C.S.L., Seumois, G., Vijayanand, P., Sette, A., and Peters, B. (2020). The Challenge of Distinguishing Cell–Cell Complexes from Singlet Cells in Non-Imaging Flow Cytometry and Single-Cell Sorting. Cytom. Part A *97*, 1127–1135. 10.1002/cyto.a.24027.
31. Simoni, Y., Becht, E., Fehlings, M., Loh, C.Y., Koo, S.-L., Teng, K.W.W., Yeong, J.P.S., Nahar, R., Zhang, T., Kared, H., et al. (2018). Bystander CD8+ T cells are abundant and phenotypically distinct in human tumour infiltrates. Nature *557*, 1–21. 10.1038/s41586-018-0130-2.
32. Paz-Ares, L.G., Ciuleanu, T.-E., Pluzanski, A., Lee, J.-S., Gainor, J.F., Otterson, G.A., Audigier-Valette, C., Ready, N., Schenker, M., Linardou, H., et al. (2023). Safety of First-Line Nivolumab Plus Ipilimumab in Patients With Metastatic NSCLC: A Pooled Analysis of CheckMate 227, CheckMate 568, and CheckMate 817. J Thorac Oncol *18*, 79–92. 10.1016/j.jtho.2022.08.014.
33. Hedrick, C.C., and Malanchi, I. (2022). Neutrophils in cancer: heterogeneous and multifaceted. Nat. Rev. Immunol. *22*, 173–187. 10.1038/s41577-021-00571-6.
34. Wculek, S.K., and Malanchi, I. (2015). Neutrophils support lung colonization of metastasis-initiating breast cancer cells. Nature *528*, 413–417. 10.1038/nature16140.
35. Saini, M., Szczerba, B.M., and Aceto, N. (2019). Circulating Tumor Cell-Neutrophil Tango along the Metastatic Process. Cancer Res. *79*, 6067–6073. 10.1158/0008-5472.can-19-1972.
36. Szczerba, B.M., Castro-Giner, F., Vetter, M., Krol, I., Gkountela, S., Landin, J., Scheidmann, M.C., Donato, C., Scherrer, R., Singer, J., et al. (2019). Neutrophils escort circulating tumour cells to enable cell cycle progression. Nature *566*, 553–557. 10.1038/s41586-019-0915-y.
37. Templeton, A.J., McNamara, M.G., Šeruga, B., Vera-Badillo, F.E., Aneja, P., Ocaña, A., Leibowitz-Amit, R., Sonpavde, G., Knox, J.J., Tran, B., et al. (2014). Prognostic Role of

Neutrophil-to-Lymphocyte Ratio in Solid Tumors: A Systematic Review and Meta-Analysis. JNCI: J. Natl. Cancer Inst. *106*, dju124. 10.1093/jnci/dju124.

38. Rayes, R.F., Mouhanna, J.G., Nicolau, I., Bourdeau, F., Giannias, B., Rousseau, S., Quail, D., Walsh, L., Sangwan, V., Bertos, N., et al. (2019). Primary tumors induce neutrophil extracellular traps with targetable metastasis promoting effects. JCI Insight *4*, e128008. 10.1172/jci.insight.128008.

39. Moreira-Teixeira, L., Stimpson, P.J., Stavropoulos, E., Hadebe, S., Chakravarty, P., Ioannou, M., Aramburu, I.V., Herbert, E., Priestnall, S.L., Suarez-Bonnet, A., et al. (2020). Type I IFN exacerbates disease in tuberculosis-susceptible mice by inducing neutrophil-mediated lung inflammation and NETosis. Nat. Commun. *11*, 5566. 10.1038/s41467-020-19412-6.

40. Yu, R., Zhu, B., and Chen, D. (2022). Type I interferon-mediated tumor immunity and its role in immunotherapy. Cell. Mol. Life Sci. *79*, 191. 10.1007/s00018-022-04219-z.

41. Zitvogel, L., Galluzzi, L., Kepp, O., Smyth, M.J., and Kroemer, G. (2015). Type I interferons in anticancer immunity. Nat. Rev. Immunol. *15*, 405–414. 10.1038/nri3845.

42. Qiu, J., Xu, B., Ye, D., Ren, D., Wang, S., Benci, J.L., Xu, Y., Ishwaran, H., Beltra, J.-C., Wherry, E.J., et al. (2023). Cancer cells resistant to immune checkpoint blockade acquire interferon-associated epigenetic memory to sustain T cell dysfunction. Nat Cancer *4*, 43–61. 10.1038/s43018-022-00490-y.

43. Jacquelot, N., Yamazaki, T., Roberti, M.P., Duong, C.P.M., Andrews, M.C., Verlingue, L., Ferrere, G., Becharef, S., Vétizou, M., Daillère, R., et al. (2019). Sustained Type I interferon signaling as a mechanism of resistance to PD-1 blockade. Cell Res. *29*, 846–861. 10.1038/s41422-019-0224-x.

44. Rybchenko, V.S., Panina, A.A., Aliev, T.K., Solopova, O.N., Balabashin, D.S., Novoseletsky, V.N., Dolgikh, D.A., Sveshnikov, P.G., and Kirpichnikov, M.P. (2021). Bispecific Antibodies for IFN-β Delivery to ErbB2+ Tumors. Biomolecules *11*, 1915. 10.3390/biom11121915.

45. Dickson, R.P., Erb-Downward, J.R., Martinez, F.J., and Huffnagle, G.B. (2015). The Microbiome and the Respiratory Tract. Annu. Rev. Physiol. *78*, 1–24. 10.1146/annurev-physiol-021115-105238.

46. Hsu-Kim, C., Hoag, J.B., Cheng, G.-S., and Lund, M.E. (2013). The Microbiology of Postobstructive Pneumonia in Lung Cancer Patients. J. Bronchol. Interv. Pulmonol. *20*, 266–270. 10.1097/lbr.0b013e31829ddf01.

47. Littman, A.J., Jackson, L.A., and Vaughan, T.L. (2005). Chlamydia pneumoniae and Lung Cancer: Epidemiologic Evidence. Cancer Epidemiology Prev. Biomark. *14*, 773–778. 10.1158/1055-9965.epi-04-0599.

48. Jin, C., Lagoudas, G.K., Zhao, C., Bullman, S., Bhutkar, A., Hu, B., Ameh, S., Sandel, D., Liang, X.S., Mazzilli, S., et al. (2019). Commensal Microbiota Promote Lung Cancer Development via γδ T Cells. Cell *176*, 998-1013.e16. 10.1016/j.cell.2018.12.040.

49. Tekle, G.E., and Garrett, W.S. (2023). Bacteria in cancer initiation, promotion and progression. Nat. Rev. Cancer *23*, 600–618. 10.1038/s41568-023-00594-2.

50. Preibisch, S., Saalfeld, S., and Tomancak, P. (2009). Globally optimal stitching of tiled 3D microscopic image acquisitions. Bioinformatics *25*, 1463–1465. 10.1093/bioinformatics/btp184.

51. Valen, D.A.V., Kudo, T., Lane, K.M., Macklin, D.N., Quach, N.T., DeFelice, M.M., Maayan, I., Tanouchi, Y., Ashley, E.A., and Covert, M.W. (2016). Deep Learning Automates the Quantitative Analysis of Individual Cells in Live-Cell Imaging Experiments. PLoS Comput. Biol. *12*, e1005177. 10.1371/journal.pcbi.1005177.

52. Liu, N., Bhuva, D.D., Mohamed, A., Bokelund, M., Kulasinghe, A., Tan, C.W., and Davis, M.J. (2023). standR: spatial transcriptomic analysis for GeoMx DSP data. Nucleic Acids Res. *52*, e2–e2. 10.1093/nar/gkad1026.

53. Robinson, M.D., and Oshlack, A. (2010). A scaling normalization method for differential expression analysis of RNA-seq data. Genome Biol. *11*, R25. 10.1186/gb-2010-11-3-r25.

54. Law, C.W., Chen, Y., Shi, W., and Smyth, G.K. (2014). voom: Precision weights unlock linear model analysis tools for RNA-seq read counts. Genome Biol. *15*, R29. 10.1186/gb-2014-15-2-r29.

55. Robinson, M.D., McCarthy, D.J., and Smyth, G.K. (2009). edgeR: a Bioconductor package for differential expression analysis of digital gene expression data. Bioinformatics *26*, 139–140. 10.1093/bioinformatics/btp616.

56. Smyth, G.K. (2011). Linear Models and Empirical Bayes Methods for Assessing Differential Expression in Microarray Experiments. Statistical Applications in Genetics and Molecular Biology *3*, 1–25. 10.2202/1544-6115.1027.

57. Phipson, B., Lee, S., Majewski, I.J., Alexander, W.S., and Smyth, G.K. (2016). Robust hyperparameter estimation protects against hypervariable genes and improves power to detect differential expression. Ann. Appl. Stat. *10*, 946–963. 10.1214/16-aoas920.

58. Y, B.Y.H. (1995). Controlling_The_False_Discovery_Rate_-_A_Practical. statistical *57*, 289–300. 10.2307/2346101.

59. McCarthy, D.J., and Smyth, G.K. (2009). Testing significance relative to a fold-change threshold is a TREAT. Bioinformatics *25*, 765–771. 10.1093/bioinformatics/btp053.
60. Liberzon, A., Birger, C., Thorvaldsdóttir, H., Ghandi, M., Mesirov, J.P., and Tamayo, P. (2015). The Molecular Signatures Database Hallmark Gene Set Collection. Cell Syst. *1*, 417–425. 10.1016/j.cels.2015.12.004.
61. Wu, D., and Smyth, G.K. (2012). Camera: a competitive gene set test accounting for inter-gene correlation. Nucleic Acids Res. *40*, e133–e133. 10.1093/nar/gks461.
62. Ritchie, M.E., Phipson, B., Wu, D., Hu, Y., Law, C.W., Shi, W., and Smyth, G.K. (2015). limma powers differential expression analyses for RNA-sequencing and microarray studies. Nucleic Acids Res *43*, e47–e47. 10.1093/nar/gkv007.
63. Phipson, B., Sim, C.B., Porrello, E.R., Hewitt, A.W., Powell, J., and Oshlack, A. (2022). propeller: testing for differences in cell type proportions in single cell data. Bioinformatics *38*, 4720–4726. 10.1093/bioinformatics/btac582.

A

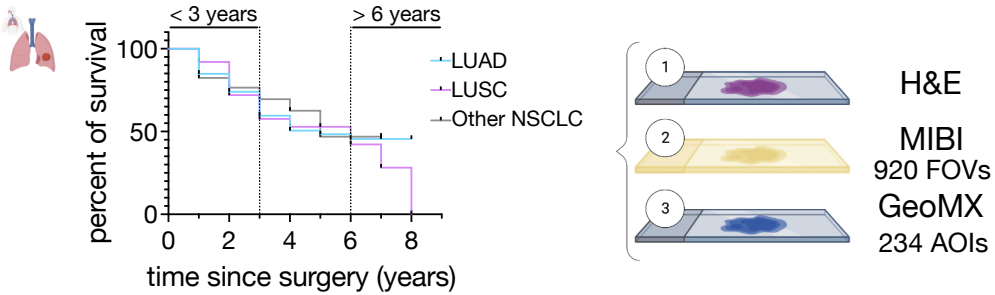
< 3 years
> 6 years
percent of survival
100
50
0
0
2
4
6
8
time since surgery (years)
LUAD
LUSC
Other NSCLC
1
2
3
H&E
MIBI
920 FOVs
GeoMX
234 AOIs

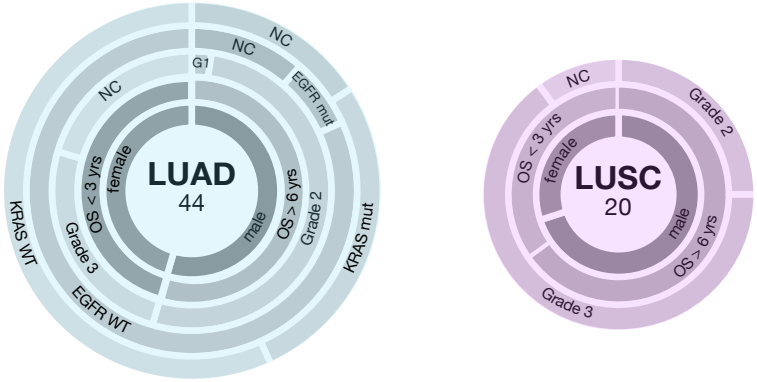
LUAD
44
female
male
OS < 3 yrs
OS > 6 yrs
Grade 2
Grade 3
KRAS WT
KRAS mut
EGFR WT
EGFR mut
NC
G1
LUSC
20
OS < 3 yrs
OS > 6 yrs
Grade 2
Grade 3
NC

B

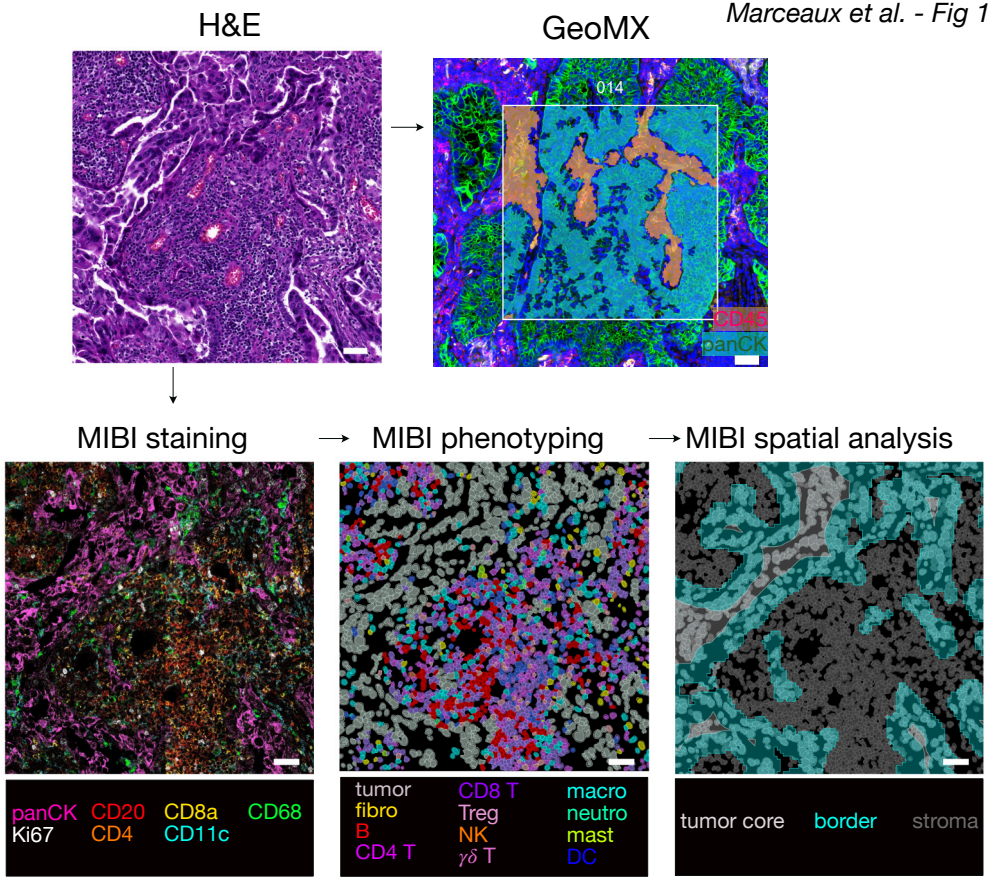
H&E
GeoMX
014
CD45
panCK
MIBI staining
MIBI phenotyping
MIBI spatial analysis
panCK
CD20
CD8a
CD68
Ki67
CD4
CD11c
tumor
fibro
B
CD4 T
CD8 T
Treg
NK
γδ T
macro
neutro
mast
DC
tumor core
border
stroma

C

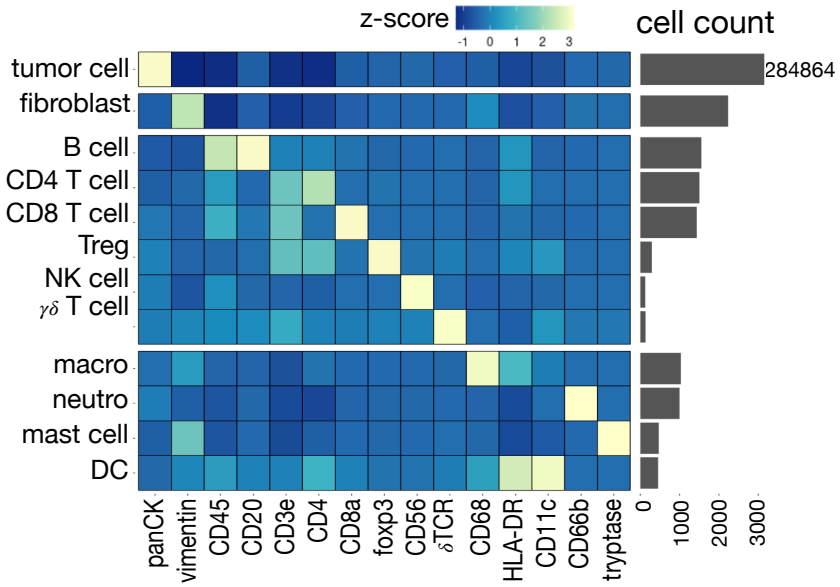
z-score
-1
0
1
2
3
cell count
tumor cell
fibroblast
B cell
CD4 T cell
CD8 T cell
Treg
NK cell
γδ T cell
macro
neutro
mast cell
DC
284864
panCK
vimentin
CD45
CD20
CD3e
CD4
CD8a
foxp3
CD56
δTCR
CD68
HLA-DR
CD11c
CD66b
tryptase
0
1000
2000
3000

D

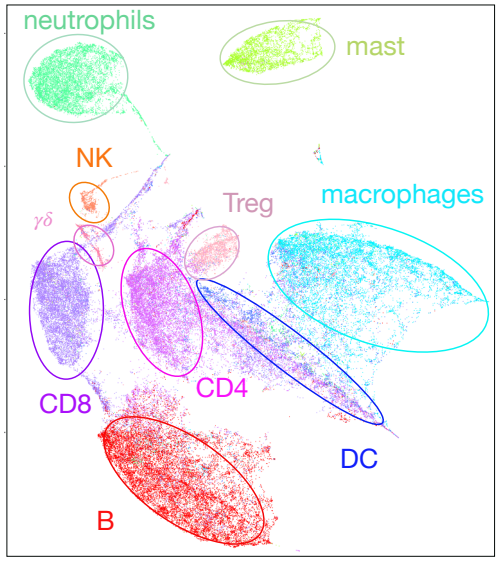
neutrophils
mast
NK
γδ
Treg
macrophages
CD8
CD4
DC
B

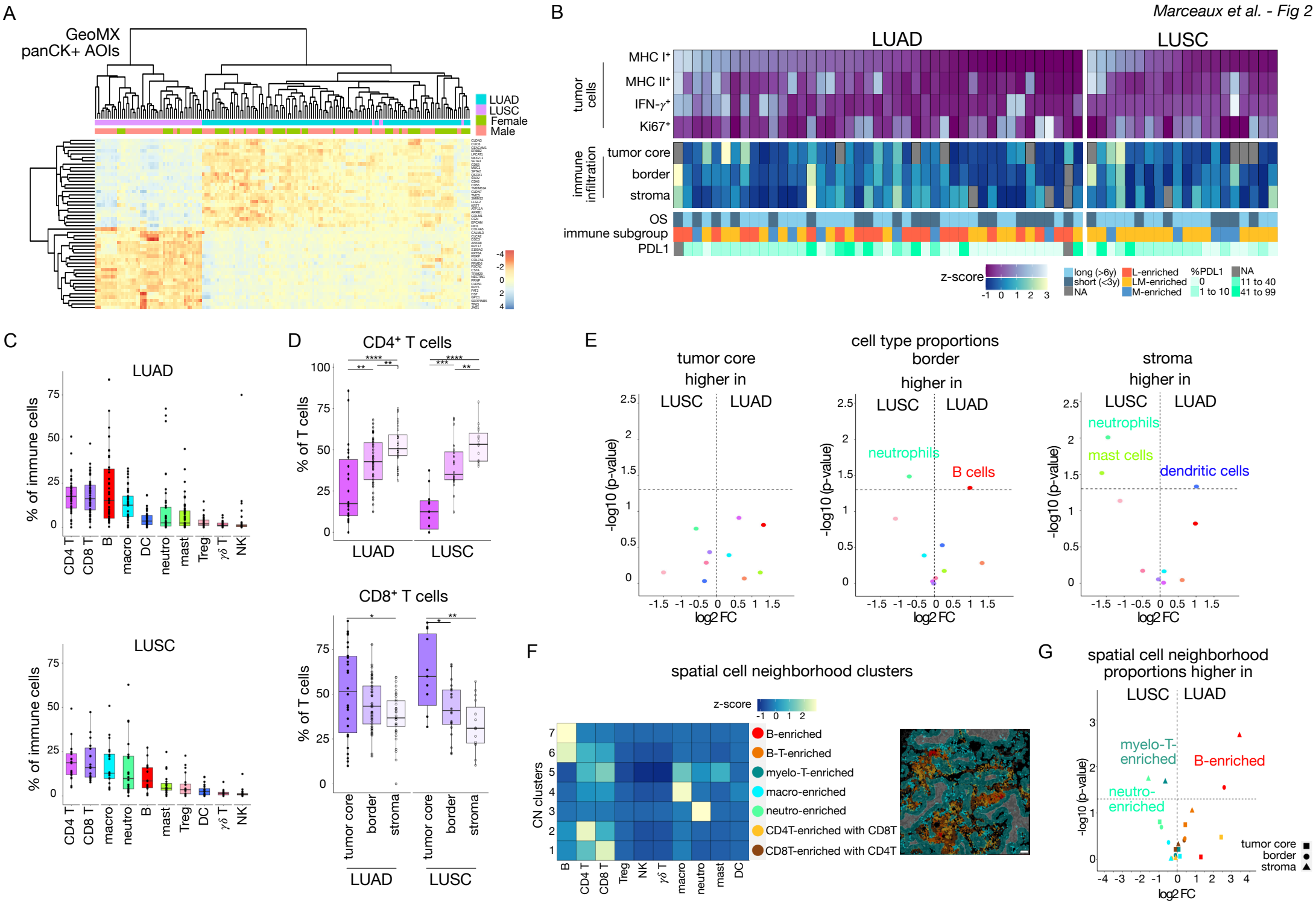
A
GeoMX
panCK+ AOIs
LUAD
LUSC
Female
Male
B
LUAD
LUSC
tumor cells
MHC I+
MHC II+
IFN-γ+
Ki67+
immune infiltration
tumor core
border
stroma
OS
immune subgroup
PDL1
z-score
long (>6y)
short (<3y)
NA
L-enriched
LM-enriched
M-enriched
%PDL1
0
1 to 10
11 to 40
41 to 99
C
LUAD
LUSC
% of immune cells
CD4 T
CD8 T
B
macro
DC
neutro
mast
Treg
γδ T
NK
D
CD4+ T cells
CD8+ T cells
% of T cells
tumor core
border
stroma
E
cell type proportions
tumor core
higher in
LUSC
LUAD
border
higher in
stroma
higher in
-log10 (p-value)
log2 FC
neutrophils
mast cells
B cells
dendritic cells
F
spatial cell neighborhood clusters
z-score
CN clusters
B-enriched
B-T-enriched
myelo-T-enriched
macro-enriched
neutro-enriched
CD4T-enriched with CD8T
CD8T-enriched with CD4T
G
spatial cell neighborhood
proportions higher in
myelo-T-
enriched
B-enriched
neutro-
enriched
tumor core
border
stroma

A

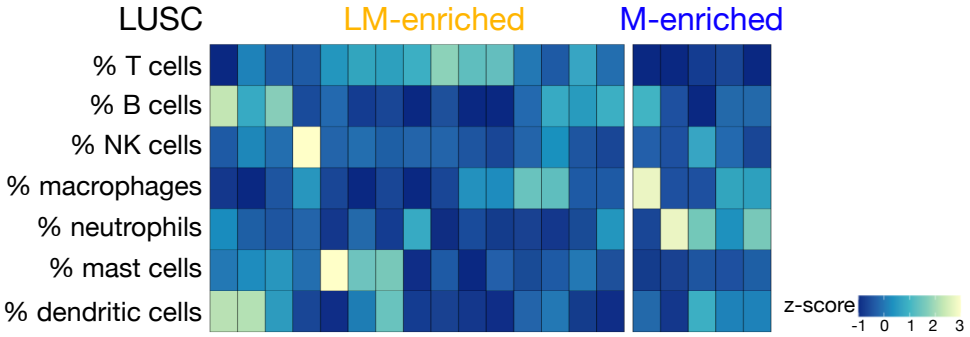
LUSC
LM-enriched
M-enriched
% T cells
% B cells
% NK cells
% macrophages
% neutrophils
% mast cells
% dendritic cells
z-score
-1 0 1 2 3

B

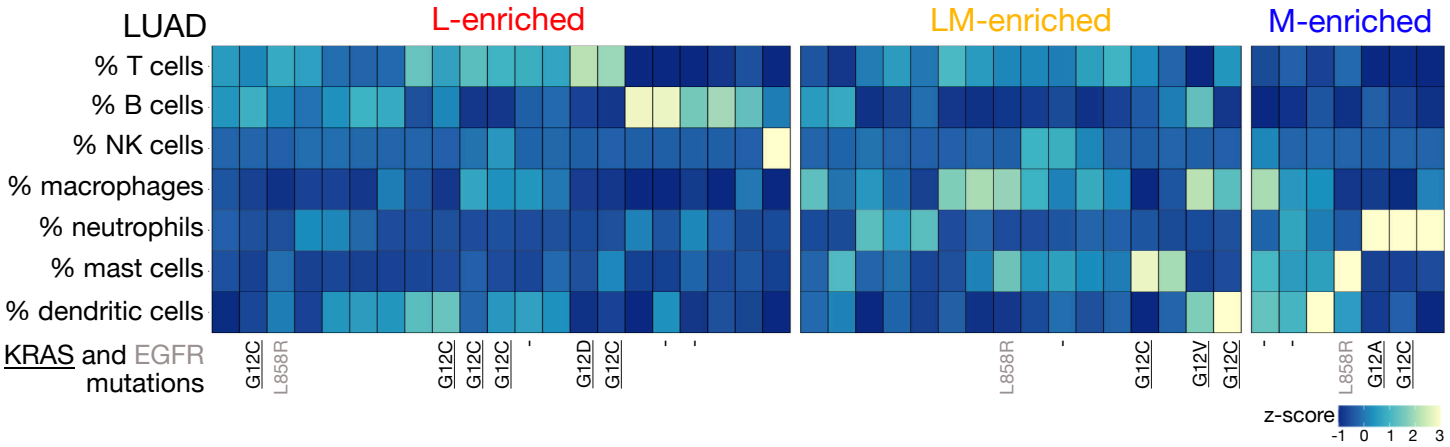
LUAD
L-enriched
LM-enriched
M-enriched
% T cells
% B cells
% NK cells
% macrophages
% neutrophils
% mast cells
% dendritic cells
KRAS and EGFR mutations
G12C
L858R
G12C
G12C
G12C
G12D
G12C
L858R
G12C
G12V
G12C
L858R
G12A
G12C
z-score
-1 0 1 2 3

C

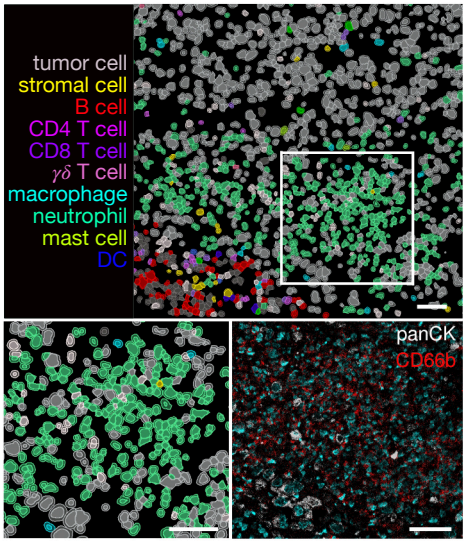
tumor cell
stromal cell
B cell
CD4 T cell
CD8 T cell
γδ T cell
macrophage
neutrophil
mast cell
DC
panCK
CD66b

D

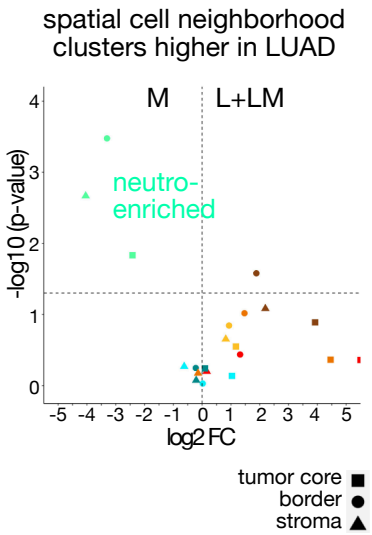
spatial cell neighborhood clusters higher in LUAD
M
L+LM
neutro-enriched
-log10 (p-value)
log2 FC
tumor core
border
stroma

E

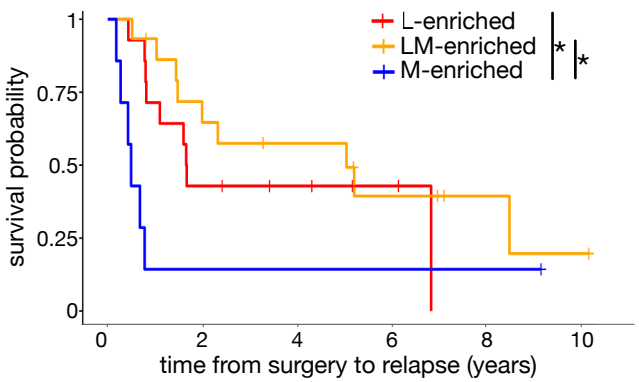
LUAD
L-enriched
LM-enriched
M-enriched
survival probability
time from surgery to relapse (years)

F

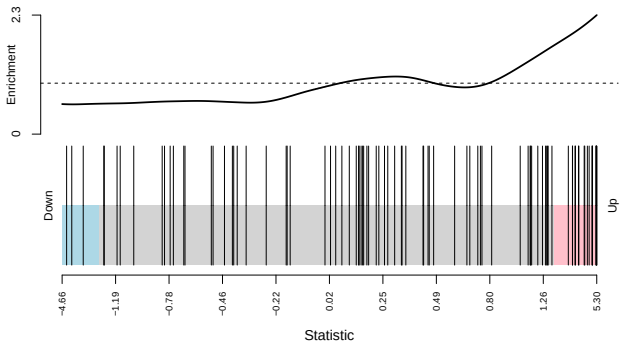
response to type I interferon in M-enriched LUAD
Enrichment
Down
Up
Statistic

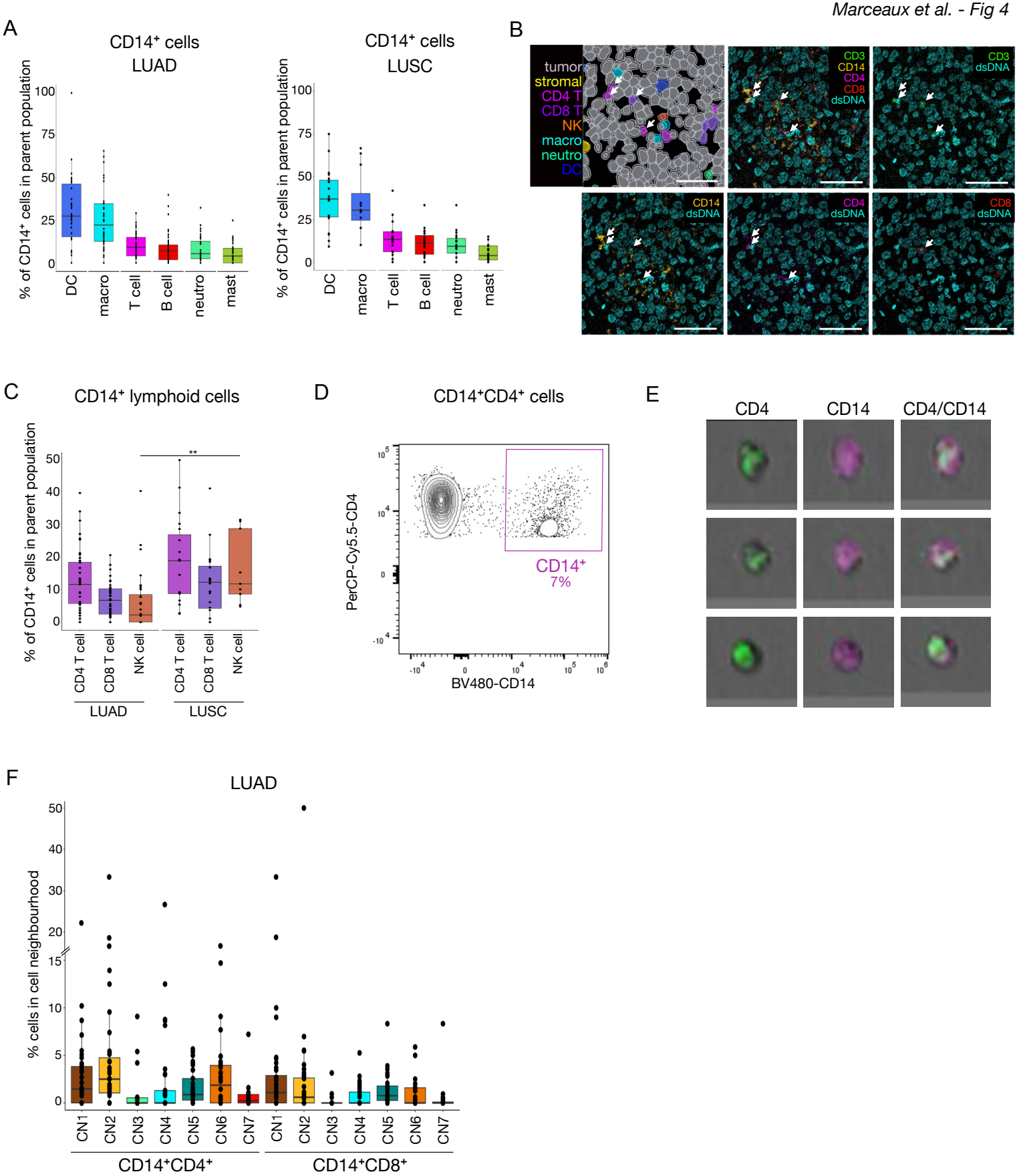
A
CD14⁺ cells
LUAD
% of CD14⁺ cells in parent population
100
75
50
25
0
DC
macro
T cell
B cell
neutro
mast
CD14⁺ cells
LUSC
B
tumor
stromal
CD4 T
CD8 T
NK
macro
neutro
DC
CD3
CD14
CD4
CD8
dsDNA
CD3
dsDNA
CD14
dsDNA
CD4
dsDNA
CD8
dsDNA
C
CD14⁺ lymphoid cells
**
CD4 T cell
CD8 T cell
NK cell
LUAD
LUSC
D
CD14⁺CD4⁺ cells
PerCP-Cy5.5-CD4
BV480-CD14
CD14⁺
7%
E
CD4
CD14
CD4/CD14
F
LUAD
% cells in cell neighbourhood
CN1
CN2
CN3
CN4
CN5
CN6
CN7
CD14⁺CD4⁺
CD14⁺CD8⁺

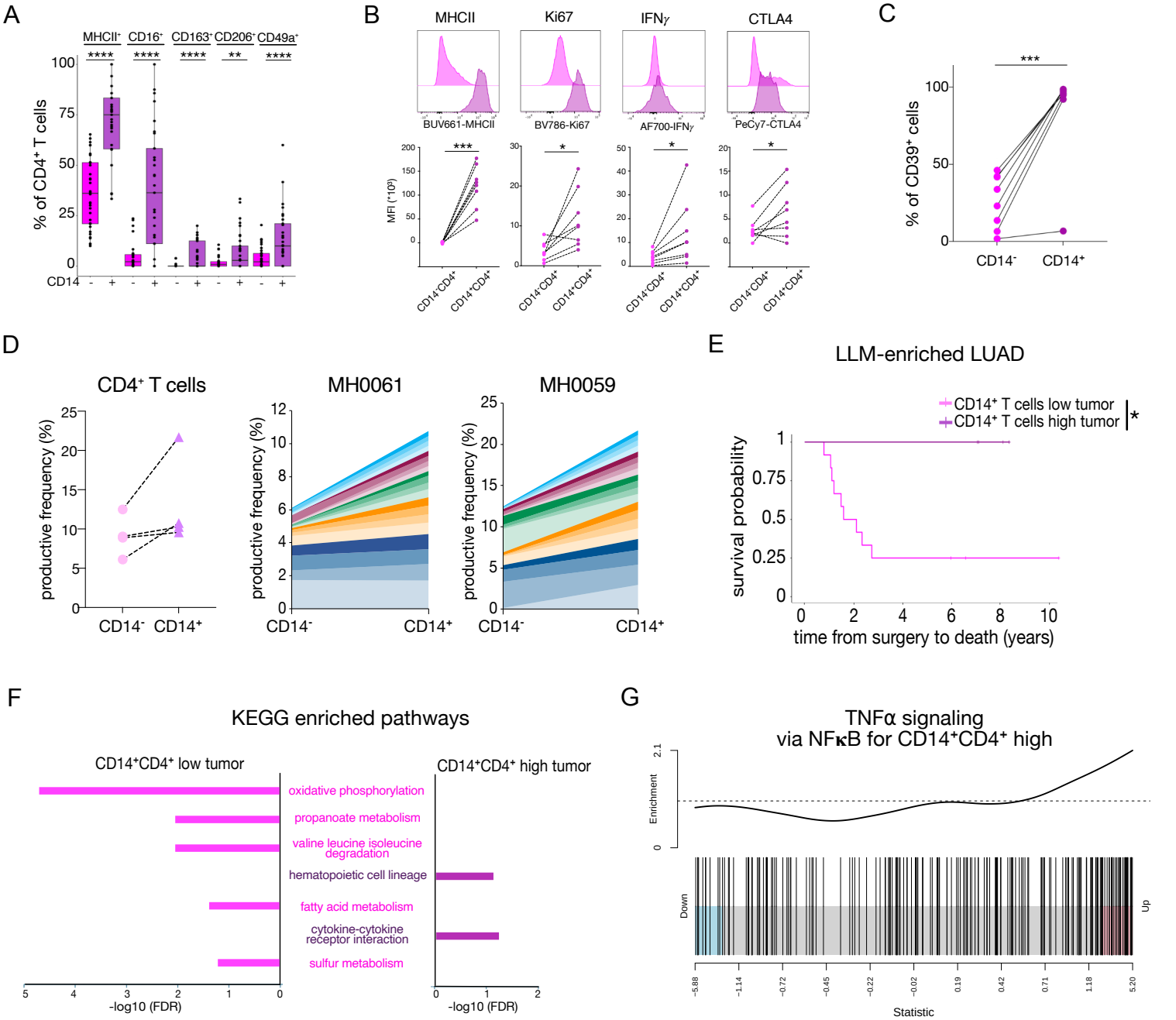
A
MHCII+ CD16+ CD163+ CD206+ CD49a+
% of CD4+ T cells
CD14
B
MHCII
Ki67
IFNγ
CTLA4
BUV661-MHCII
BV786-Ki67
AF700-IFNγ
PeCy7-CTLA4
MFI (*10⁶)
CD14-CD4+
CD14+CD4+
C
% of CD39+ cells
CD14-
CD14+
D
CD4+ T cells
MH0061
MH0059
productive frequency (%)
CD14-
CD14+
E
LLM-enriched LUAD
CD14+ T cells low tumor
CD14+ T cells high tumor
survival probability
time from surgery to death (years)
F
KEGG enriched pathways
CD14+CD4+ low tumor
CD14+CD4+ high tumor
oxidative phosphorylation
propanoate metabolism
valine leucine isoleucine degradation
hematopoietic cell lineage
fatty acid metabolism
cytokine-cytokine receptor interaction
sulfur metabolism
-log10 (FDR)
G
TNFα signaling via NFκB for CD14+CD4+ high
Enrichment
Down
Up
Statistic